Cite as: R. R. Herrick, S. Hensley, *Science* 10.1126/science.abm7735 (2023).

# Surface changes observed on a Venusian volcano during the Magellan mission

**Robert R. Herrick[1]* and Scott Hensley[2]**

[1]Geophysical Institute, University of Alaska Fairbanks, Fairbanks, AK 99775, USA. [2]Jet Propulsion Laboratory, California Institute of Technology, Pasadena, CA 91109, USA.

*Corresponding author. Email: rrherrick@alaska.edu

**Venus has a geologically young surface, but it is unknown whether it has ongoing active volcanism. From 1990 to 1992, the Magellan spacecraft imaged the planet's surface using synthetic aperture radar. We examine volcanic areas on Venus that were imaged two or three times by Magellan and identify a ~2.2 km$^2$ volcanic vent that changed shape in the eight months between two radar images. Additional volcanic flows downhill from the vent are visible in the second epoch images, though we cannot rule out that they were present but invisible in the first epoch due to differences in imaging geometry. We interpret these results as ongoing volcanic activity on Venus.**

Venus is nearly the same size and mass as Earth. Compositional constraints are consistent with Venus having an Earth-like abundance of radioactive elements, which release heat that might drive volcanic activity (*1*). The number of impact craters on Venus indicates a mean surface age of a few hundred million years (*2*). However, many of the craters have morphologies that appear to have been modified by volcanic processes; if so, it could mean the average surface age is only tens of millions of years, as young as Earth's ocean basins (*3*). The vast majority of Earth's volcanism is associated with crust formation at mid-ocean ridges or volcanic arcs above subduction zones. Venus does not have current plate tectonics (*4*). Geodynamic models of Venus that match the geological and geophysical observations disagree on the expected current level of volcanism, producing various predictions that it could be lower than, the same as, or many times higher than the level of hot spot volcanism on Earth (*5*–*9*).

On Earth, the Hawaiian volcanic hot spot erupts every few years (*10*, *11*). There are several dozen volcanoes on Venus with sizes (*12*) and gravity signatures indicative of underlying hot mantle plumes (*13*) larger than Hawaii's Big Island (*14*). It has been predicted (*15*) that multiple basaltic eruptions might occur over the course of a Venusian sidereal day (243 Earth days). Extending this analogy predicts lava flow areas covering several tens of kilometers over the same period (*10*, *11*, *16*).

## Magellan radar images

From 1990 to 1992 the Magellan spacecraft (*17*) imaged the surface of Venus using synthetic aperture radar (SAR), at a resolution of 100-300 m. Data were recorded in overlapping swaths taken on the descending passes of the spacecraft's highly elliptical orbit, such that a given surface location was imaged once per sidereal day as the planet rotated. Images were acquired over sets of three sidereal days, referred to as cycles. Cycle 1 observed ~84% of the planet with east-looking SAR images. Cycle 2 filled gaps from Cycle 1 and acquired second images for ~35% of the planet using west-looking SAR. ~15% of Venus was imaged again during Cycle 3, which also acquired east-looking images, generally at an incidence angle (the angle from vertical with which the SAR beam intersects the surface) differing by ~20° from that used in Cycle 1. Because ~8% of the planet was imaged in all three cycles, a total of ~42% of the global surface area was imaged two or more times.

The different imaging geometries used for each cycle are not conducive to automated methods of searching for changes due to volcanic activity. We therefore performed a manual search of areas previously identified as most likely to possess active volcanism (*18*–*20*). The areas that we searched include large volcanoes in a published database (*12*) that also have geoid anomalies (a distortion of the planet's equipotential surface) greater than 15 m, topographic rises (*20*), coronae considered to be active in another database (*19*), and shield volcanoes in (*18*) that were evaluated as likely being active. Table S1 summarizes the areas that we searched. We restricted the search to areas that were imaged multiple times. Our goal was to identify volcanic constructs that appeared or were altered between the images, such as volcanic cones, vents, or lava flows.

We examined full-resolution Magellan images of each area of interest, looking for changes in geologic features between cycles (*21*). Whenever we interpreted a feature as having changed, we used stereo radargrammetry to produce a topographic model for the area surrounding the feature and to orthorectify the images (*21*). Stereo radargrammetry applies stereo photogrammetry techniques to SAR images. Terrain variations in a scene cause changes in the relative position of features in images taken from two different perspectives, which are exploited to derive the topography. The original images were then altered to appear as if the viewpoint was directly overhead (orthorectification). We then used the stereo-derived topography and the orthorectified images to interpret the nature and potential cause of the observed

change in appearance. We evaluated the viability of each interpretation using a simple geometric model of the feature, which we developed using forward modeling of the Cycle 1 image (*21*). The model was used to simulate the appearance of the feature under the different viewing geometries (*21*), which were qualitatively compared to the Cycle 2 and/or 3 images.

**An active vent in Atla Regio**

Figure 1 shows gridded Magellan altimetry overlain on Magellan Cycle 1 SAR images of an area in Atla Regio, Venus. It extends from 9° S, 170° W to 6.25° N, 151° W, an area of ~$3.2\times10^6$ km$^2$. This area contains two of the planet's largest volcanoes, Ozza and Maat Mons, which have previously been hypothesized to be locations of active volcanism (*22*–*24*). Magellan observed this area with east-looking images in Cycle 1 (incidence angle 45°) and west-looking images in Cycle 2 (incidence angle 25°). This area has not been imaged by Earth-based radar or during the earlier Venera 15 and Venera 16 missions to Venus.

We identified a volcanic vent at 1.363° N, 165.359° W that changed shape and expanded (Fig. 2) in the eight-month interval between the Magellan imaging in Cycles 1 and 2 (February to October 1991). The vent is located on the north side of a domed shield volcano that is part of the larger Maat Mons volcano (*23*). In the east-looking Cycle 1 image, the vent appears near-circular (1.5 × 1.8 km, area 2.2 km$^2$) with steep interior slopes. We speculate that it was a drained post-eruptive vent. In the west-looking Cycle 2 image, the vent has become larger (4.0 km$^2$) and irregular in shape. In Cycle 2 the vent wall, identifiable as bright pixels on the vent's west side (an east-facing slope) and dark pixels on east side (west-facing slope), is narrow, so the vent interior and exterior are separated by only a few pixels in the 75 meters per pixel radar mosaic. We interpret this as due to short vent walls, perhaps only tens of meters high, which implies that the vent is nearly filled to its rim in the Cycle 2 image. We speculate that a lava lake formed in the vent interior during the 8-month gap between images.

To provide regional context, we identified matching points in the Cycle 1 and 2 images and used them to generate relative elevations and to orthorectify the images (*21*). The results are shown in Fig. 2C-D. The Cycle 2 image contains a set of radar-bright flows, downhill and to the north of the vent, that are not visible in the Cycle 1 image. However, the topographic relief of the flows is not resolved by the Magellan data, and the two radar images were taken at different incidence angles. We therefore cannot exclude the possibility that the flows were present when the Cycle 1 image was taken, but were not apparent in the image, perhaps because the surface texture makes the flows more distinguishable at the lower incidence angle of Cycle 2. The surface area of the flows is 69 km$^2$, consistent with typical hot spot volcanism on Earth. For comparison, the 2018 Kīlauea Puna eruption in Hawaii covered an area of ~35 km$^2$ (*25*), and the associated caldera collapse atop Kīlauea (~500 m drop) had an area of ~5 km$^2$ (*26*).

A vent atop a volcano could expand because either i) an influx of magma disrupts, fills, and expands the vent; or ii) an underlying magma chamber could drain, causing the vent to expand by partial collapse. The lack of visible topographic features within the enlarged vent in the Cycle 2 images is consistent with a fluid (e.g. lava) having filled the vent to a hydrostatic level. However, the image resolution is insufficient to rule out the interior of the vent being filled with debris at the time of Cycle 2, rather than by an active or cooled lava lake. It is possible that the increase in vent size was caused only by collapse, rather than magmatism. If collapse occurred, it could potentially have been caused by withdrawal of magma from a chamber below the vent to feed a nearby eruption. The flows to the north might have been fed by an unresolved vent, rather than directly from the vent that changed in size. Regardless of the cause, we definitively conclude that the vent has changed. We are not aware of an Earth analogue for multi-kilometer changes to a volcanic vent occurring with no accompanying volcanism, but we cannot rule out this possibility for this Venusian vent.

No newly formed volcanic constructs, such as a small shield or a cinder cone, were identified in this study area or in regions that were previously surveyed (table S1).

**Comparison with simulations**

To check our interpretation, we constructed a simple model (*21*) of a vent as a circular, flat-floored rimless pit, to match the observed vent in the Cycle 1 imaging conditions. We then examined how the model pit would appear under Cycle 2 observation conditions, and compared the model to the observed Cycle 2 image (Fig. 3). We applied the same modeling approach to another vent of similar size just to the north, which we interpreted as unchanged between the two observations (vent U, Fig. 3). The models of the changed vent (vent V, Fig. 3) and vent U had rim radii $r_b$ of 850 m and 1070 m, respectively, with varying depths and steepness of the walls. We used a simple analytic function (*21*) to describe smooth walls extending from the pit rim to a flat floor, of floor radius $r_f$. We varied the vent depth $D$ from 175 to 675 m in increments of 125 m for vent V, and from 175 to 875 m in increments of 175 m for vent U. The different increment sizes were chosen to produce the same change in wall slope angles, given the differing vent radii. We varied the steepness of the walls in the model by varying the floor radii from 400 to 625 m (shallowest and steepest interior slopes respectively) in increments of 75 m for the changed vent and from 500 to 800 m in increments of 100 m for vent U. We also simulated west-east terrain slopes $\tau_{xt}$ of 0°, 5°, 10° and 25° (positive slope upward to the east). The simulation incorporated a variety of radar imaging effects associated with noise and terrain variation (*21*). The simulated appearances of all these models are shown in figs. S5 to S9. Varying the depths and slopes of the model vent changes the width and magnitude of

shadowing, foreshortening, and layover. Varying the west-east slope causes the width of a pit rim to appear differently between opposite-look images and changes the apparent elongation in the west-east direction.

For the changed vent, the simulation that visually most resembles the Cycle 1 image was a pit with depth 175 m and floor radius 625 m on a 5° west-facing slope (Fig. 3). This is consistent with the surrounding stereo-derived topography from manual match-point selection (Fig. 2), and provides some west-east elongation of the vent in Cycle 2. The visual indicators used to assess whether the model was similar to the observed Cycle 1 image were the size and shape of the shadow region on the west side of the interior of the vent, the shape and magnitude of the layover region on the east side of the interior of the vent, and the ellipticity of the vent rim. The latter was quantified using the ratio of north-south to east-west vent diameters. The cross-track slope was assessed using a comparison of mean image brightness between the Cycle 1 and Cycle 2 images. The simulated 5° west-facing slope is consistent with the mean image brightness difference observed between the Cycle 1 and Cycle 2 images in an area just to the west of the vent. The observed difference is 0.9 dB, while the simulated 5° west-facing slope has 1.5 dB difference (*21*); the corresponding simulated values for 0° and 10° are 3 dB and 0 dB respectively.

The observed Cycle 2 image of vent V is substantially different from the simulation (Fig 3). The observed Cycle 2 image does not show elongated shadowing on the east side; the elongation of the simulated vent in the east-west direction is less than the observed elongation; the simulation has a prominent foreshortened bright western wall that is not present in the observed image; and the simulation cannot reproduce the vent's kidney-shape as viewed from above. There is no large shadowed region associated with the vent's eastern wall in the observed Cycle 2 image, indicating that the vent became shallower than it was at the time of the Cycle 1 image. For comparison, our model of vent U matches its appearance and mean backscatter in both imaging cycles using a pit of depth 175 m, rim radius 1070 m, and floor radius 800 m, on a west-facing slope of 0° (Fig. 3). The bright backscatter arc to the east of vent U (not included in the models) is due to an east-facing slope of 15˚-20˚, inferred from the difference between Cycle 1 and 2 backscatter values.

**Implications for volcanism on Venus**

With only one changed feature, we cannot determine how common currently active volcanism is on Venus. We draw a distinction between identifying recent volcanism on a planet (*23*, *27*, *28*) and demonstrating that it is currently volcanically active. For example, Mars has lava flows with estimated ages of less than a few million years (*29*, *30*), but no volcanic activity has been identified over multiple decades of continuous observation. Only one feature has been identified in our survey of the Magellan data, and none in kilometer-scale radar observations from Earth that covered ~25% of Venus' surface (*31*). The low detection rate indicates that Venus is less volcanically active than Jupiter's moon Io, for which over 100 active spots have been imaged (*32*). We estimate that our search of the Magellan data has examined ~1.5% of Venus' surface area (table S1), accounting for missing and poor data. The changed vent is located in a region where volcanic activity was thought to be most likely (*22*, *23*). Our results make it unlikely that volcanism on Venus has dwindled to a small fraction of Earth's activity over the last few hundred million years (*5*, *7*), but there are a wide range of possible activity scenarios that are compatible with Hawaiian-like levels of volcanism in Atla Regio.

**REFERENCES AND NOTES**


1. V. L. Barsukov, A. T. Basilevsky, V. P. Volkov, V. N. Zharkov, *Venus Geology, Geochemistry, and Geophysics: Research Results from the USSR.* (Univ. of Arizona Press, 1992).
2. R. J. Phillips, R. F. Raubertas, R. E. Arvidson, I. C. Sarkar, R. R. Herrick, N. Izenberg, R. E. Grimm, Impact craters and Venus resurfacing history. *J. Geophys. Res.* **97**, 15923–15948 (1992). doi:10.1029/92JE01696
3. R. R. Herrick, M. E. Rumpf, Postimpact modification by volcanic or tectonic processes as the rule, not the exception, for Venusian craters. *J. Geophys. Res. Planets* **116**, E02004 (2011).
4. S. C. Solomon, S. E. Smrekar, D. L. Bindschadler, R. E. Grimm, W. M. Kaula, G. E. McGill, R. J. Phillips, R. S. Saunders, G. Schubert, S. W. Squyres, E. R. Stofan, Venus tectonics: An overview of Magellan observations. *J. Geophys. Res.* **97**, 13199–13255 (1992). doi:10.1029/92JE01418
5. R. G. Strom, G. G. Schaber, D. D. Dawson, The global resurfacing of Venus. *J. Geophys. Res*. **99**, 10899–10926 (1994). doi:10.1029/94JE00388
6. P. K. Byrne, R. C. Ghail, A. M. C. Şengör, P. B. James, C. Klimczak, S. C. Solomon, A globally fragmented and mobile lithosphere on Venus. *Proc. Natl. Acad. Sci. U.S.A.* **118**, e2025919118 (2021). doi:10.1073/pnas.2025919118 Medline
7. A. T. Basilevsky, J. W. Head, Venus: Timing and rates of geologic activity. *Geology* **30**, 1015–1018 (2002). doi:10.1130/0091-7613(2002)030<1015:VTAROG>2.0.CO;2
8. V. S. Solomatov, L.-N. Moresi, Stagnant lid convection on Venus. *J. Geophys. Res.* **101** , 4737–4753 (1996). doi:10.1029/95JE03361
9. J. E. Guest, E. R. Stofan, A new view of the stratigraphic history of Venus. *Icarus* **139**, 55–66 (1999). doi:10.1006/icar.1999.6091
10. F. W. Klein, Patterns of historical eruptions at Hawaiian volcanoes. *J. Volcanol. Geotherm. Res.* **12**, 1–35 (1982). doi:10.1016/0377-0273(82)90002-6
11. R. I. Tilling, C. Heliker, D. A. Swanson, *Eruptions of Hawaiian Volcanoes: Past, Present, and Future* (US Geological Survey, 2010).
12. L. S. Crumpler, J. C. Aubele, D. A. Senske, S. T. Keddie, K. P. Magee, J. W. Head, "Volcanoes and centers of volcanism on Venus," in *Venus II: Geology, Geophysics, Atmosphere, and Solar Wind Environment*, S. W. Bougher, D. M. Hunten, R. J. Phillips, Eds. (Univ. of Arizona Press, 1997), pp. 697–756.
13. A. S. Konopliv, W. B. Banerdt, W. L. Sjogren, Venus Gravity: 180th Degree and Order Model. *Icarus* **139**, 3–18 (1999). doi:10.1006/icar.1999.6086
14. M. Monnereau, A. Cazenave, Depth and geoid anomalies over oceanic hotspot swells: A global survey. *J. Geophys. Res.* **95**, 15429–15438 (1990). doi:10.1029/JB095iB10p15429
15. R. D. Lorenz, Probabilistic constraints from existing and future radar imaging on volcanic activity on Venus. *Planet. Space Sci.* **117**, 356–361 (2015). doi:10.1016/j.pss.2015.07.009
16. C. A. Neal, S. R. Brantley, L. Antolik, J. L. Babb, M. Burgess, K. Calles, M. Cappos, J. C. Chang, S. Conway, L. Desmither, P. Dotray, T. Elias, P. Fukunaga, S. Fuke, I. A. Johanson, K. Kamibayashi, J. Kauahikaua, R. L. Lee, S. Pekalib, A. Miklius, W. Million, C. J. Moniz, P. A. Nadeau, P. Okubo, C. Parcheta, M. R. Patrick, B. Shiro, D. A. Swanson, W. Tollett, F. Trusdell, E. F. Younger, M. H. Zoeller, E. K. Montgomery-Brown, K. R. Anderson, M. P. Poland, J. L. Ball, J. Bard, M. Coombs, H. R. Dietterich, C. Kern, W. A. Thelen, P. F. Cervelli, T. Orr, B. F. Houghton, C. Gansecki, R. Hazlett, P. Lundgren, A. K. Diefenbach, A. H. Lerner,

G. Waite, P. Kelly, L. Clor, C. Werner, K. Mulliken, G. Fisher, D. Damby, The 2018 rift eruption and summit collapse of Kīlauea Volcano. *Science* **363**, 367–374 (2019). doi:10.1126/science.aav7046 Medline
17. R. S. Saunders, A. J. Spear, P. C. Allin, R. S. Austin, A. L. Berman, R. C. Chandlee, J. Clark, A. V. Decharon, E. M. De Jong, D. G. Griffith, J. M. Gunn, S. Hensley, W. T. K. Johnson, C. E. Kirby, K. S. Leung, D. T. Lyons, G. A. Michaels, J. Miller, R. B. Morris, A. D. Morrison, R. G. Piereson, J. F. Scott, S. J. Shaffer, J. P. Slonski, E. R. Stofan, T. W. Thompson, S. D. Wall, Magellan mission summary. *J. Geophys. Res.* **97**, 13067–13090 (1992). doi:10.1029/92JE01397
18. R. R. Herrick, J. Dufek, P. J. McGovern, Evolution of large shield volcanoes on Venus. *J. Geophys. Res. Planets* **110**, E01002 (2005).
19. A. J. P. Gülcher, T. V. Gerya, L. G. J. Montési, J. Munch, Corona structures driven by plume–lithosphere interactions and evidence for ongoing plume activity on Venus. *Nat. Geosci.* **13**, 547–554 (2020). doi:10.1038/s41561-020-0606-1
20. E. R. Stofan, S. E. Smrekar, "Large topographic rises, coronae, large flow fields, and large volcanoes on Venus: Evidence for mantle plumes?" in *Plates, Plumes, and Paradigms*, G. R. Foulger , J. H. Natland , D. C. Presnall , D. L. Anderson, Eds. (Geological Society of America, 2005), vol. 388, pp. 841–857.
21. Materials and methods are available as supplementary materials.
22. J. Brossier, M. S. Gilmore, K. Toner, A. J. Stein, Distinct Mineralogy and Age of Individual Lava Flows in Atla Regio, Venus Derived From Magellan Radar Emissivity. *J. Geophys. Res. Planets* **126**, e2020JE006722 (2021). doi:10.1029/2020JE006722 Medline
23. C. A. Robinson, J. A. Wood, Recent Volcanic Activity on Venus: Evidence from Radiothermal Emissivity Measurements. *Icarus* **102**, 26–39 (1993). doi:10.1006/icar.1993.1030
24. R. J. Phillips, Estimating lithospheric properties at Atla Regio, Venus. *Icarus* **112**, 147–170 (1994). doi:10.1006/icar.1994.1175
25. P. Lundgren, M. Bagnardi, H. Dietterich, Topographic Changes During the 2018 Kīlauea Eruption From Single-Pass Airborne InSAR. *Geophys. Res. Lett.* **46**, 9554–9562 (2019). doi:10.1029/2019GL083501
26. D. R. Shelly, W. A. Thelen, Anatomy of a Caldera Collapse: Kīlauea 2018 Summit Seismicity Sequence in High Resolution. *Geophys. Res. Lett.* **46**, 14395–14403 (2019). doi:10.1029/2019GL085636
27. E. R. Stofan, S. E. Smrekar, N. Mueller, J. Helbert, Themis Regio, Venus: Evidence for recent (?) volcanism from VIRTIS data. *Icarus* **271**, 375–386 (2016). doi:10.1016/j.icarus.2016.01.034
28. S. E. Smrekar, E. R. Stofan, N. Mueller, A. Treiman, L. Elkins-Tanton, J. Helbert, G. Piccioni, P. Drossart, Recent hotspot volcanism on Venus from VIRTIS emissivity data. *Science* **328**, 605–608 (2010). doi:10.1126/science.1186785 Medline
29. W. K. Hartmann, D. C. Berman, Elysium Planitia lava flows: Crater count chronology and geological implications. *J. Geophys. Res.* **105**, 15011–15025 (2000). doi:10.1029/1999JE001189
30. D. G. Horvath, P. Moitra, C. W. Hamilton, R. A. Craddock, J. C. Andrews-Hanna, Evidence for geologically recent explosive volcanism in Elysium Planitia, Mars. *Icarus* **365**, 114499 (2021). doi:10.1016/j.icarus.2021.114499
31. B. A. Campbell, D. B. Campbell, "The Earth-Based Radar Search for Volcanic Activity on Venus" in *52nd Lunar and Planetary Science Conference*, 15 to 19 March 2021 (LPSC, 2021), 2339.
32. P. E. Geissler, Volcanic Activity on Io During the Galileo Era. *Annu. Rev. Earth Planet. Sci.* **31**, 175–211 (2003). doi:10.1146/annurev.earth.31.100901.145428
33. S. Hensley, Model Code and Datasets for Science Magellan Surface Change Paper, version 1, Dataverse (2023); https://doi.org/10.48577/jpl.U5IBW5.
34. J. J. Plaut, "Stereo imaging" in *Guide to Magellan Image Interpretation* (JPL Publication 93-24, NASA and JPL, 1993), pp. 33–43.
35. F. Leberl, *Radargrammetric Image Processing* (Artech House, 1989).
36. S. Hensley, "A combined methodology for SAR interferometric and stereometric error modeling" in *2009 IEEE Radar Conference*, Pasadena, CA, 4 to 8 May 2009 (IEEE, 2009), pp. 1–6.

**ACKNOWLEDGMENTS**

We thank B. Grimm, J. Whitten, S. Smrekar, B. Campbell, and Z. Haddad for comments that improved the content, as did comments from three anonymous reviewers. **Funding:** S.H. was funded by NASA contract 80NM0020F0035. **Author contributions:** R.R.H. searched for changes in the Magellan images, generated the stereo-derived topography and orthorectified the images, and contributed the geologic interpretation. S.H. provided an independent check of the stereo-derived topography and performed the simulations. Both authors wrote sections of the paper. **Competing interests:** The authors declare that they have no competing interests. **Data and materials availability:** Four Magellan datasets were used, all available through NASA's Planetary Data System Annex: mosaic of the Cycle 1 images: https://astrogeology.usgs.gov/search/map/Venus/Magellan/Venus_Magellan_LeftLook_mosaic_global_75m; Cycle 2 mosaic: https://astrogeology.usgs.gov/search/map/Venus/Magellan/Venus_Magellan_RightLook_mosaic_global_75m; Cycle 3 mosaic: https://astrogeology.usgs.gov/search/map/Venus/Magellan/Venus_Magellan_StereoLook_mosaic_global_75m; and a global mosaic of Magellan gridded altimetry: https://astrogeology.usgs.gov/search/map/Venus/Magellan/RadarProperties/Venus_Magellan_Topography_Global_4641m_v02. The modeling source code and output files are available through the Jet Propulsion Laboratory Dataverse (*33*). **License information:** Copyright © 2023 the authors, some rights reserved; exclusive licensee American Association for the Advancement of Science. No claim to original US government works. https://www.science.org/about/science-licenses-journal-article-reuse

**SUPPLEMENTARY MATERIALS**

science.org/doi/10.1126/science.abm7735
Materials and Methods
Supplementary Text
Figs. S1 to S9
Table S1
References (*34*–*36*)

Submitted 11 October 2021; accepted 21 February 2023
Published online 15 March 2023
10.1126/science.abm7735

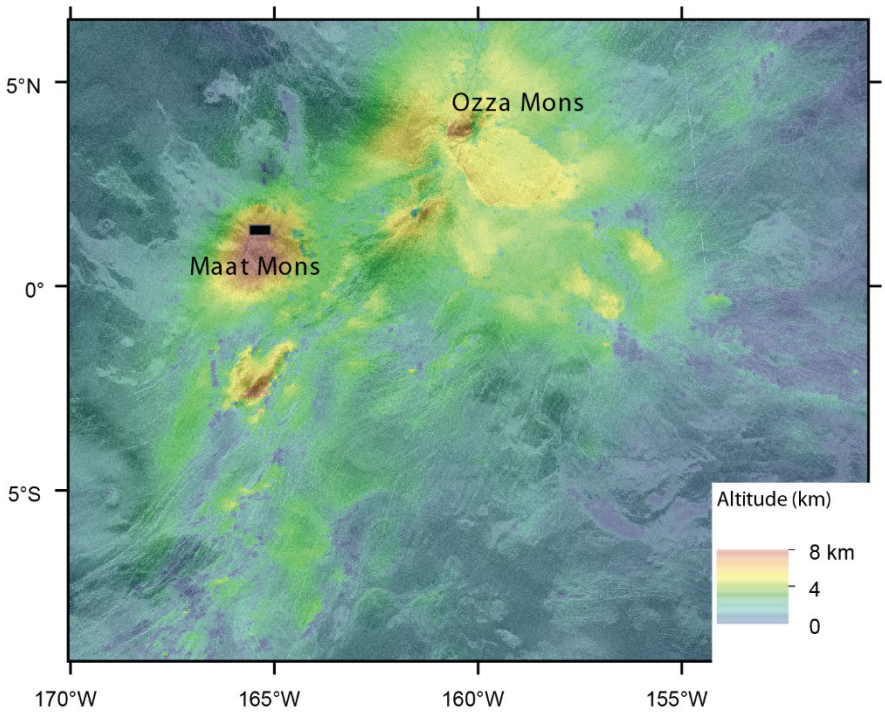


**Fig. 1. Topography and SAR image of the Study area on Venus.** Color indicates elevations, measured relative to the mean planetary radius from gridded Magellan altimetry. X and Y axis are planetary longitude and latitude. The background greyscale image is Cycle 1 east-looking SAR images. The black rectangle indicates the area shown in Fig. 2.

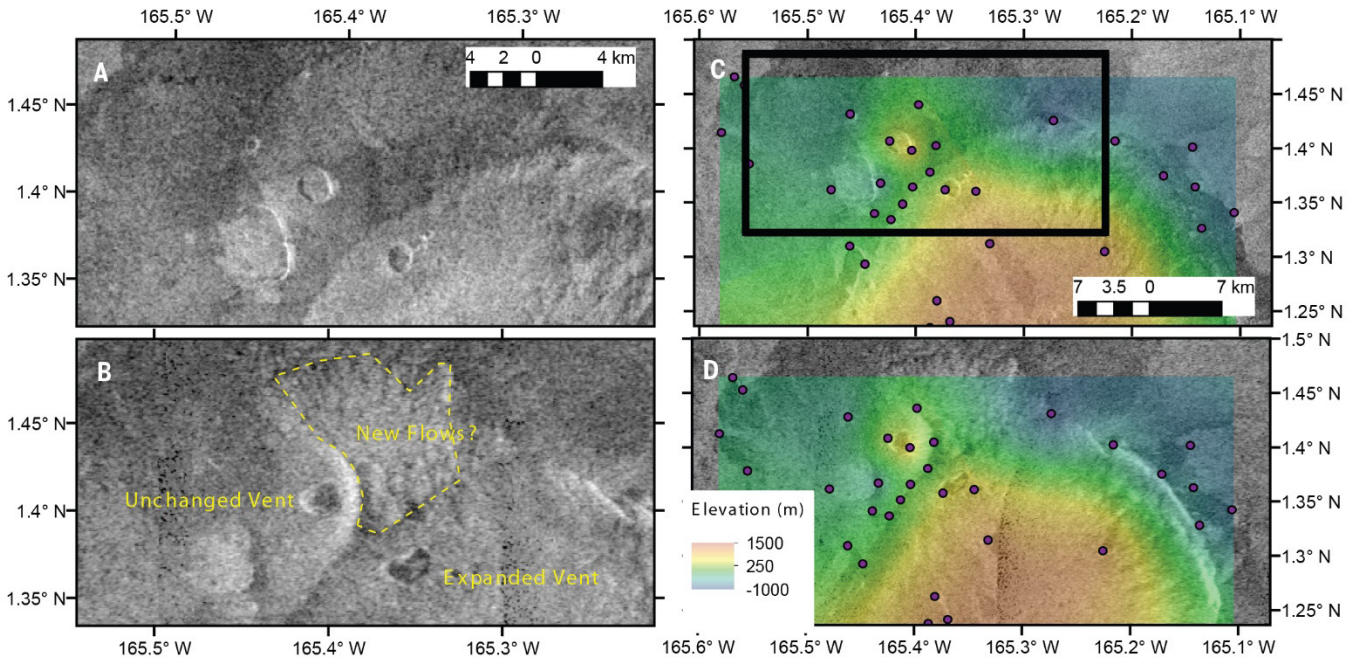


**Fig. 2. Radar images of a vent which has changed shape.** (**A**) east-looking Cycle 1 and (**B**) west-looking Cycle 2 images of the changed vent and its surroundings. In the Cycle 1 image the vent appears nearly circular and deep with steep walls. In Cycle 2 the vent appears larger, irregular in outline, shallower and nearly filled. The dashed yellow line outlines radar-bright lava flows visible in the Cycle 2 image that were not apparent in Cycle 1. (**C** and **D**) The same images indicating the manually selected match points (purple dots) that were used to generate relative elevations (overlain in color) and to orthorectify the images. The black box in (C) indicates the extent of the unrectified images shown in panels A and B. All images are in a sinusoidal projection, using a projection longitude of 165.359°W.

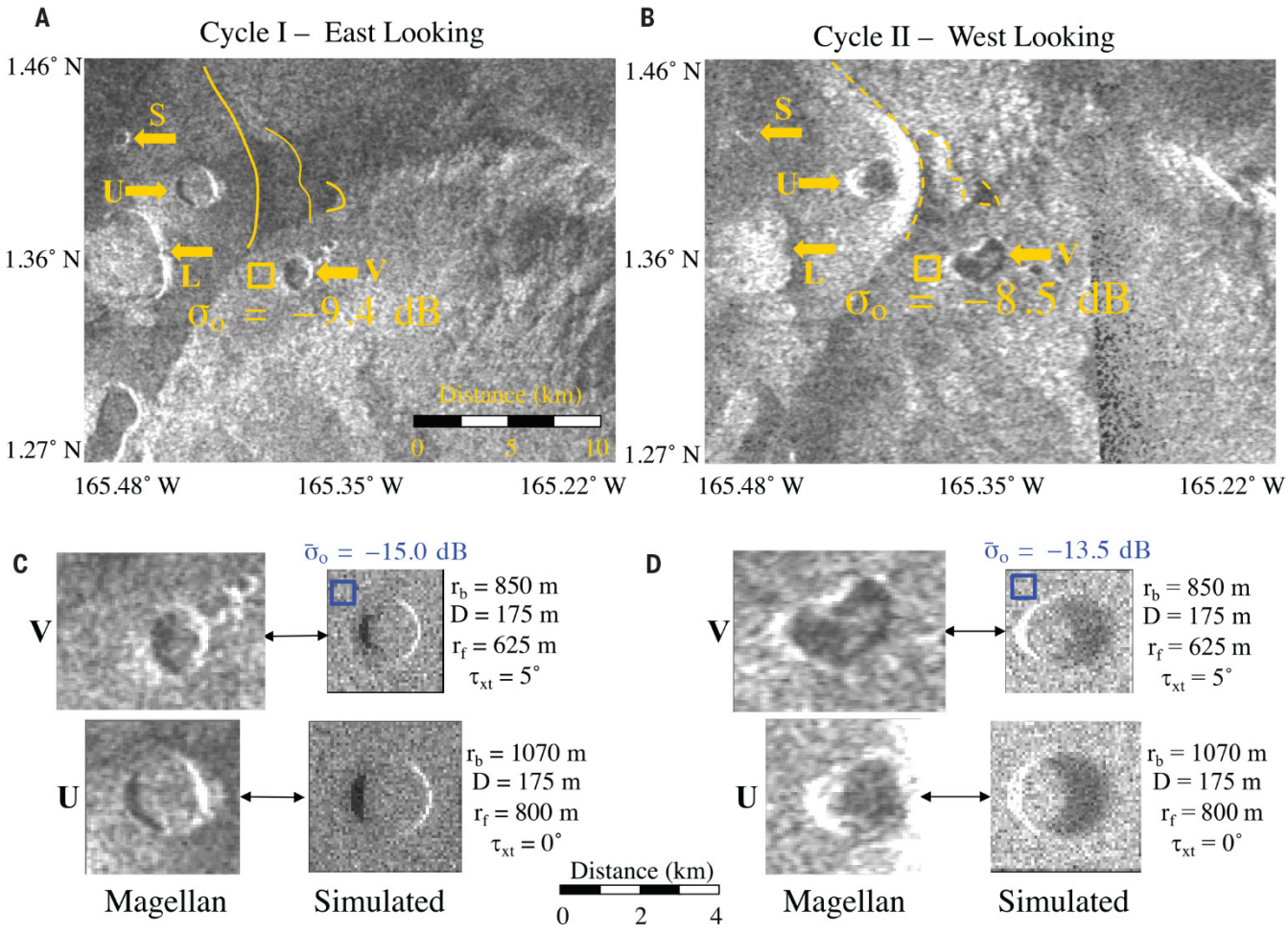


**Fig. 3. Comparison between the observations and simulated appearances of model vents.** Radar images acquired in (**A**) Cycle 1 and (**B**) Cycle 2, indicating the changed vent (labeled V) and an unchanged vent (labeled U). Also visible are a smaller vent (labeled S) and ridge (labeled L). Scale bar in panel A also applies to panel B. The yellow lines are interpreted as breaks in topographic slope in Cycle 1 (solid lines) and Cycle 2 (dotted lines), within the area of the potential lava flow. Yellow rectangles indicate the regions used to compute the mean backscatter level for the terrain surrounding vent V in the Magellan data; the resulting values are labeled. (**C**) Simulated appearances of model vents, with geometries selected to appear similarly to the two vents in Cycle 1, shown as zoomed cut-outs from panel A for comparison. The mean backscatter in the simulated data was measured in the blue box, with the resulting value labeled. The parameters of each model are labelled. Scale bar applies to panels C and D. (**D**) The same models as they would appear in the Cycle 2 images, compared to cut-outs from panel B. The simulated model is consistent with the observations of vent U, but does not match vent V in either geometry or radiometry.